

Investigation on the Effect of Nozzle Number on the Recirculation Rate and Mixing Time in the RH Process Using VOF + DPM Model



HAITAO LING, FEI LI, LIFENG ZHANG, and ALBERTO N. CONEJO

A mathematical model has been developed to explain the effect of the number of nozzles on recirculation flow rate in the RH process. Experimental data from water modeling were employed to validate the mathematical model. The experimental data included the velocity fields measured with a particle image velocimetry technique and mixing time. The multiphase model volume of fluid was employed to allow a more realistic representation of the free surface in the vacuum chamber while injected argon bubbles were treated as discrete phase particles and modeled using the discrete phase model. Interfacial forces between bubbles and liquid phase were considered, including the lift force. The simulations carried out with the mathematical model involved changes in the gas flow rate from 12 to 36 L/min and a number of nozzles from 4 to 8. The results indicated a logarithmic increment in the recirculation rate as the gas flow rate increased and also corresponded with an exponential decrease in mixing time. The plume area and liquid velocities resulting from individual nozzles were computed. A maximum optimum recirculation rate was defined based on a mechanism proposed to explain the effect of gas flow rate and the number of nozzles on the recirculation rate.

DOI: 10.1007/s11663-016-0669-y

© The Minerals, Metals & Materials Society and ASM International 2016

I. INTRODUCTION

AS a metallurgical reactor, the Ruhrstahl-Heraeus (RH) degasser consists of a ladle, a vacuum chamber, an up-leg snorkel, and a down-leg snorkel. Several nozzles are distributed along the circumference of the up-leg snorkel. During RH refining, the temperature is approximately 1823 K (1550 °C) and the phases of molten steel, molten slag, and argon gas are involved. The molten steel from the up-leg snorkel rises to a certain height due to the pressure difference between the vacuum chamber and the atmosphere. The argon gas from the nozzles is injected into the up-leg snorkel and expands when heated. Hence, the density of the mixture decreases and the molten steel is driven to flow into the vacuum chamber along the up-leg snorkel. At the same time, part of the molten steel from the down-leg snorkel flows towards the ladle. In actual operations, RH steel refining is widely used for decarburization, deoxidization, desulfurization, temperature control, inclusion removal, and homogenization of chemical composition.

With the limitations of high temperature, multiphase system, and vacuum conditions, the metallurgical processes in the RH degasser are hardly observed and tested. In general, the numerical simulation and water modeling are used to study and visualize this fundamental phenomenon in the RH degasser.^[1-4] In numerical simulation, a series of multiphase flow models like the VOF model, the Mixture model, the Eulerian model, etc. can be solved to predict the velocity distribution of the molten steel, the volume fraction of the gas, and the interfacial behavior among different phases. Furthermore, water and air are the phases employed to simulate molten steel and argon in water modeling. The models can be either at a reduced scale or at full scale. The dynamic similarity must first be satisfied in a reduced scale model.^[5,6] It requires that the modified Froude number in the model should be equivalent to that in the prototype.

The flow of molten steel has a direct effect on the refining efficiency of the RH degasser. The key parameters include the recirculation rate and mixing time that are regarded as the dominant factors influencing the decarburization rate. Due to the increasing demand for ultra-low carbon steels, it is very important to improve our current understanding on fluid flow and mixing phenomena in the RH process.

The recirculation rate and mixing time depend on many variables, such as gas flow rate, vacuum pressure, height of liquid steel in the vacuum chamber, snorkel immersion depth, snorkel diameter, the number of nozzles, its diameter, and its the injection angle. The recirculation rate increases with a higher gas flow rate,^[1-3,7-10] lower vacuum pressure,^[1] larger immersion depth,^[1,7,11] and larger snorkel diameter.^[1,11,12] Han *et al.*^[13] reported a

HAITAO LING and FEI LI, Ph.D. Students, and LIFENG ZHANG, Professor, are with the Beijing Key Laboratory of Green Recycling and Extraction of Metals (GREM), and also with the School of Metallurgical and Ecological Engineering, University of Science and Technology Beijing (USTB), Beijing 100083, P.R. China. Contact e-mail: zhanglifeng@ustb.edu.cn ALBERTO N. CONEJO, formerly Visiting Professor with the School of Metallurgical and Ecological Engineering, University of Science and Technology Beijing (USTB), is now Professor with the Graduate Program in Metallurgy, Morelia Technological Institute, Morelia, Mexico.

Manuscript submitted December 22, 2015.

Article published online April 4, 2016.

maximum recirculation flow rate for an injection angle of 12 deg. Nascimento *et al.*^[14] reported an increase in recirculation rate as the nozzle diameter increased, a result contrary to more recent reports.^[15,16]

The effect of the number of nozzles on the recirculation rate in the RH process has been investigated in the past^[1,9,14,17–20] and is summarized in Table I. In previous investigations, it has been found that increasing the number of nozzles, the recirculation rate increases. In general, it has been reported that above an optimum number of nozzles the recirculation rate remains constant or even decreases. The optimum number of nozzles was different in previous reports, suggesting the importance of additional work in this field.

Computational fluid dynamics (CFD) tools have been employed in the past to describe mixing phenomena in metallurgical ladles under multiphase flow conditions.^[3,7,8,21–24] The motion of the continuous phase and dispersed phase is treated with different numerical methods. The volume of fraction (VOF) method is frequently used to describe the motion of the continuous phase and the coupling between the continuous and dispersed phase.^[21–23,25,26] The discrete particle method (DPM) can be used to describe the motion of the discrete phase.^[3,7,8,24,27–36] In most of this previous work, the free surface is assumed to be flat. By this assumption, the fluctuation of the interface, slag-eye formation, and slag entrainment can hardly be tracked.

The objective of this work is to investigate the effect of the number of nozzles on both recirculation rate and mixing time and provide additional information to understand the behavior of fluid flow and mixing phenomena as a function of the number of nozzles. A mathematical model combining VOF and DPM has been developed to carry out this objective, validated with experimental data obtained from measurements with PIV in a water model. The numerical model can describe fluctuations of the free surface.

II. MATHEMATICAL MODEL

In this study, the VOF model^[26] and DPM^[36] were employed to simulate fluid flow and the motion of the bubbles. The VOF model follows the Euler–Euler approach and tracks the free surface of the fluid, and the DPM model follows the Euler–Lagrange approach. Air bubbles were treated as the discrete phase in water and the top gas phase. The top gas phase was treated as a second continuous phase. The basic equations are as follows.

A. VOF Model

The tracking of the interface between the air phase in the vacuum chamber and the liquid phase is accomplished by the solution of a continuity equation for the volume fraction of each phase. For the gas phase, this equation has the following form

$$\frac{1}{\rho_g} \left[\frac{\partial}{\partial t} (\alpha_g \rho_g) + \nabla \cdot (\alpha_g \rho_g \vec{v}_g) \right] = 0 \quad [1]$$

where α_g is the volume fraction of gas, ρ_g is the density of gas, \vec{v}_g is the gas velocity.

The volume fraction of the primary phase is solved under the following constraint.

$$\sum_{q=1}^n \alpha_q = 1 \quad [2]$$

A single momentum equation is solved throughout the domain and the resulting velocity field is shared among the phases. It is dependent on the volume fractions of all phases through the properties ρ and μ . The momentum equation is expressed by

$$\frac{\partial}{\partial t} (\rho \vec{u}_i) + \nabla \cdot (\rho \vec{u}_i \vec{u}_j) = -\nabla P + \nabla [\mu (\nabla \vec{u}_i + \nabla \vec{u}_i^T)] + \rho \vec{g} \quad [3]$$

The density and viscosity in each cell is given by

$$\rho = \alpha_g \rho_g + \alpha_l \rho_l \quad [4]$$

$$\mu = \alpha_g \mu_g + \alpha_l \mu_l, \quad [5]$$

where α_l is the volume fraction of the primary phase, u_i and u_j are the velocity of the mixture phase in the x , y , and z directions, ρ_l is the density of the primary phase, μ_g is the gas viscosity, μ_l is the viscosity of the primary phase. The standard κ – ϵ model developed by Launder and Spalding^[37] is used to simulate the turbulence parameters.

B. Discrete Particle Model (DPM)

Gas bubbles enter the liquid from the nozzles in the up-leg snorkel. The forces acting on gas bubbles include the inter-phase forces between the liquid and gas bubbles, the gravity force, and the buoyancy force. The inter-phase forces consist of the drag force, the

Table I. Summary of Previous Research on RH Including the Effect of the Number of Nozzles

	Results	N	d_0 (mm)
Inoue <i>et al.</i> ^[17]	experimental (1:8)	1, 8, 16	2
Hanna <i>et al.</i> ^[18]	experimental (1:5)	4, 6, 8, 10, 16	3
Kamata <i>et al.</i> ^[9]	experimental	1, 4, 8	1
Park <i>et al.</i> ^[11]	exp (1:10) and num	6 to 24 (ten)	4
Nascimento <i>et al.</i> ^[14]	experimental (1:5)	5, 10, 20	1.0, 1.5, 2.2, 2.8
Jiang <i>et al.</i> ^[19]	experimental	1, 4, 7	1, 3, 5
Zhu <i>et al.</i> ^[20]	exp (1:5) and num	6, 7, 8, 9, 10	1

virtual mass force, the pressure gradient force, and the lift force. Aoki *et al.*^[32] studied the motion of gas bubbles and the removal of inclusions in a 133 ton steel-refining ladle in detail, considering the above interaction forces.

The following force balance equation represents the motion of gas bubbles.

$$\frac{d\vec{u}_{b,i}}{dt} = \vec{F}_{D,i} + \vec{F}_{G,i} + \vec{F}_{B,i} + \vec{F}_{VM,i} + \vec{F}_{L,i} + \vec{F}_{P,i}, \quad [6]$$

where $u_{b,i}$ is the velocity of gas bubbles, $F_{D,i}$ is the drag force, $F_{G,i}$ is the gravity force, $F_{B,i}$ is the buoyancy force, $F_{VM,i}$ is the virtual mass force, $F_{L,i}$ is the lift force, and $F_{P,i}$ is the pressure gradient force, respectively.

1. Drag force, $F_{D,i}$

The drag force that the liquid imparts on gas bubbles depends on the Reynolds number of gas bubbles, the viscosity of the liquid, bubble size, bubble density, and the relative velocity between the liquid and the gas by following equation.

$$\vec{F}_{D,i} = \frac{3\mu_1 C_D Re_b}{4\rho_{b,i} d_{b,i}^2} (\vec{u}_l - \vec{u}_{b,i}), \quad [7]$$

where μ_1 is the viscosity of the liquid, $\rho_{b,i}$ is the density of gas bubbles, $d_{b,i}$ is the diameter of gas bubbles, Re_b is the Reynolds number of gas bubbles, and C_D is the drag coefficient. In this study, gas bubbles are assumed to be spherical and the drag coefficient is expressed by the following equation.

$$C_D = a_1 + \frac{a_2}{Re_b} + \frac{a_3}{Re_b^2}, \quad [8]$$

where a_1 , a_2 , and a_3 are constants that apply over several ranges of Re_b given by Morsi and Alexander.^[38]

The Reynolds number of gas bubbles is computed as follows:

$$Re_b = \frac{\rho_1 d_{b,i} |\vec{u}_l - \vec{u}_{b,i}|}{\mu_1}, \quad [9]$$

where ρ_1 is the density of the water and $d_{b,i}$ is the diameter of gas bubbles.

The diameter of gas bubbles is calculated from the following equation and it is assumed to be constant.^[39]

$$d_b = 0.35 \left(\frac{Q^2}{g} \right)^{0.2} \quad [10]$$

In water modeling, the gas flow rate is much less than that of the real RH degasser according to the dynamic similarity. It can be found that the bubble size is much smaller than that in the latter. The bubble size in accordance with Eq. [10] is ranged from 3.20 to 6.55 mm when the gas flow rate is 12 to 36 L/min. However, Zhang^[40] found that the average size of bubbles was 10 to 19 mm in industrial practice when nozzles, tuyeres, or porous plugs were used to introduce gas into the metallurgical vessels at gas flow rates of $(40 \text{ to } 200) \times 10^{-6} \text{ m}^3 \text{ s}^{-1}$.

2. Gravity and buoyancy force

The combined effect of the gravity and the buoyancy forces on the motion of gas bubbles in the liquid is given by the following expression:

$$\vec{F}_{G,i} + \vec{F}_{B,i} = \frac{(\rho_{b,i} - \rho_l)}{\rho_{b,i}} g \cdot \vec{e}_i, \quad [11]$$

where \vec{e}_i is unit vector.

3. Virtual mass force $F_{VM,i}$

When gas bubbles accelerate relative to the fluid, the velocity of the surrounding fluid will increase. The additional force is called the virtual mass force and is represented by the following equation.

$$\vec{F}_{VM,i} = C_{VM} \frac{\rho_l}{\rho_{b,i}} \frac{d}{dt} (\vec{u}_l - \vec{u}_{b,i}), \quad [12]$$

where C_{VM} is the virtual mass coefficient and it is set to 0.5.

4. Lift force, $F_{L,i}$

The interfacial lift force takes into consideration that the pressure at one side of the gas bubble is different from another side when there is a velocity gradient in the fluid. Méndez and Nigro^[41] reported that the effects produced by the lift force could not be neglected in a metallurgical gas stirred ladle. It can exist in the horizontal and vertical directions. So that the gas bubble rotates and moves toward the direction of velocity gradient. The lift force is defined by the following equation:

$$\vec{F}_{L,i} = C_L \frac{\rho_l}{\rho_{b,i}} (\vec{u}_l - \vec{u}_{b,i}) \times \nabla \times \vec{u}_l, \quad [13]$$

where C_L is the lift coefficients.

Drew and Passman^[42] found that C_L was 0.5 for an inviscid flow around a sphere and 0.01 for a viscous flow. Pourtousi and Sahu^[43] suggested that the lift force improved the accuracy in prediction of the axial liquid velocity, turbulent kinetic energy, and radial gas hold-up, and the lift coefficient C_L for bubbly flow regime with small spherical bubbles was in the range of 0.1 to 0.5. Zhang^[24] clearly described a better agreement with experimental data when the inter-phase lift force was not ignored. The lift coefficient C_L in the current study is defined as 0.1.

When gas bubbles flow upwards in the up-leg snorkel, there is a plume zone occupied by gas bubbles and liquid. The volume fraction of both phases are calculated by

$$\alpha_b = \frac{1}{\Delta V_{\text{cell}}} \sum_i^{N_{b,\text{cell}}} \frac{Q_{b,i}^s \Delta t}{\rho_{b,i}} \quad [14]$$

$$\alpha_l + \alpha_b = 1, \quad [15]$$

where α_b is the volume fraction of gas bubbles, α_l is the volume fraction of molten steel, ΔV_{cell} is the computational cell volume, $N_{b,\text{cell}}$ is the number of bubbles

in the computational cell, $Q_{b,i}^s$ is the flow rate of the injected bubble stream, Δt is the time step of bubble trajectory calculation.

The recirculation process of the liquid in the RH degasser is motivated by the density decrease in the up-leg snorkel. Hence, it is necessary to consider the volume fraction of the liquid when calculating the fluid flow of the liquid. The governing equations for the liquid can be derived based on the Navier–Stokes equations for single-phase flows. They are represented as:

$$\frac{\partial}{\partial t}(\alpha_l \rho_l) + \nabla \cdot (\alpha_l \rho_l \vec{u}_l) = 0 \quad [16]$$

$$\frac{\partial}{\partial t}(\alpha_l \rho_l \vec{u}_l) + \vec{u}_l \cdot \nabla (\alpha_l \rho_l \vec{u}_l) = -\nabla P + \nabla \cdot [\alpha_l (\mu_l + \mu_t)] \nabla \vec{u}_l + \vec{F}_b, \quad [17]$$

where F_b is the source term for momentum exchange with bubbles and is defined by

$$\vec{F}_b = - \sum_i^{N_{b,cell}} \left[\begin{aligned} & \frac{3\mu_l C_{D,i} Re_i}{4\rho_{b,i} d_{b,i}^2} (\vec{u}_l - \vec{u}_{b,i}) + C_{VM} \frac{\rho_l}{\rho_{b,i}} \frac{d}{dt} (\vec{u}_l - \vec{u}_{b,i}) + \\ & C_L \frac{\rho_l}{\rho_{b,i}} (\vec{u}_l - \vec{u}_{b,i}) \times \nabla \times \vec{u}_l + \frac{\rho_l}{\rho_{b,i}} \vec{u}_l \cdot \nabla \vec{u}_l \end{aligned} \right] \alpha_l Q_{b,i}^s \Delta t \quad [18]$$

The relevant parameters of Eq. [18] have been described above.

The standard κ - ε model is modified to model the turbulence due to the inter-phase exchange forces acting on the liquid phase. The corresponding equations are as follows.

$$\alpha_l \rho_l \left(\frac{\partial \kappa}{\partial t} + \vec{u}_l \cdot \nabla \kappa \right) = \nabla \cdot \left[\left(\alpha_l \frac{\mu_t}{\sigma_\kappa} \right) \nabla \kappa \right] + \alpha_l G_\kappa - \alpha_l \rho_l \varepsilon + S_\kappa \quad [19]$$

$$\alpha_l \rho_l \left(\frac{\partial \varepsilon}{\partial t} + \vec{u}_l \cdot \nabla \varepsilon \right) = \nabla \cdot \left[\left(\alpha_l \frac{\mu_t}{\sigma_\varepsilon} \right) \nabla \varepsilon \right] + \alpha_l C_{1\varepsilon} \frac{\varepsilon}{\kappa} G_\kappa - \alpha_l C_{2\varepsilon} \rho_l \frac{\varepsilon^2}{\kappa} + S_\varepsilon, \quad [20]$$

where the model constants are $C_{1\varepsilon} = 1.44$, $C_{2\varepsilon} = 1.92$, $\sigma_\kappa = 1.0$, and $\sigma_\varepsilon = 1.3$.^[37] S_κ and S_ε are the source terms for turbulent energy and its dissipation rate is caused by the motion of gas bubbles, respectively. They can be expressed as:^[32]

$$S_\kappa = \frac{C_{sk}}{\Delta V_{cell}} \sum_i^{N_{b,cell}} \frac{3\alpha_l \mu_l C_{D,i} Re_i}{4d_{b,i}^2 \rho_{b,i}} |\vec{u}_l - \vec{u}_{b,i}|^2 Q_{b,i}^2 \Delta t \quad [21]$$

$$S_\varepsilon = C_{1\varepsilon} \frac{\varepsilon}{\kappa} S_\kappa \quad [22]$$

Aoki *et al.*^[32] found that the value of C_{sk} was 0.12 and the calculated flow field showed a good agreement with the experimental data by Xie and Oeters.^[44]

Mixing time is a very important parameter during RH refining. A small cell volume is patched to be defined as the tracer at the top surface of the molten steel in the vacuum chamber once the flow field reached steady state. At the same time, variation of the tracer concentration is monitored at fifty points in the ladle. The time when the tracer concentration reaches ± 5 pct of final value (C_∞) is defined as the mixing time. Tracer transport equation is as follows.

$$\frac{\partial(\rho_l C)}{\partial t} + \nabla \cdot (\rho_l \vec{u}_l C) = \nabla \cdot \left[\frac{\mu_{eff}}{Sc} \left(\frac{\partial C}{\partial x_i} \right) \right], \quad [23]$$

where C is the tracer concentration, μ_{eff} is the effective viscosity, and Sc is the turbulent Schmidt number.

C. Boundary and Initial Conditions

The inlet velocity is calculated according to the total gas flow rate at the nozzle. Atmospheric pressure is assumed on the free surface of the ladle. The free surface is allowed to move, considering a manometric pressure in the vacuum chamber of -4802 Pa. It corresponds with a vacuum degree of 133 Pa in actual operations satisfying the dynamic similarity. Hence, the pressure in the vacuum chamber is 96,523 Pa. Non-slip conditions are chosen at the walls. The volume fraction of the air is unit at the top portion of the ladle and the vacuum chamber. Due to the same physical properties, gas bubbles move at their inherent velocity when entering the top gas phase and they are allowed to escape from the top surface of the vacuum chamber. The standard wall function is used to model the turbulence characteristics in the near-wall region. The system is assumed to be isothermally at 298 K (25 °C).

D. Computational Procedure

The system of equations was solved by combining the authors' user-defined subroutines with a commercial CFD software (Fluent version 14.0). The flowchart of the mathematical models is given in Figure 1. The optimum number of mesh cells was approximately 300,000. The convergence criterion for all variables was set to 10^{-4} . The PISO scheme was used for the pressure-velocity coupling. The time step was 0.001 seconds. All computations were performed on a Windows 7 PC with Intel 3.4GHz CPU and 8GB RAM. It took approximately 14 to 18 seconds to reach steady state. When the simulation reached steady state, the mixing time was calculated based on the velocity field. The parameters of the liquid and gas phases in the numerical simulations are listed in Table II.

III. MODEL VALIDATION

A water model with a geometric scale 1:5 from an industrial size RH unit of 210 tons was built. The

dimensions of the model and prototype are given in Tables III and IV. Pressure in the vacuum chamber was fixed at 96,523 Pa, controlled by the vacuum pump. The gas flow rate in the water model was defined using the similarity criteria based on the Modified Froude number. The immersion depth was ranged from 30 to 40 mm. Measurements on mixing time and velocity fields were carried out in order to validate the mathematical model. Mixing time was measured injecting a tracer and measuring their concentration as a function of time at the position, as indicated in Figure 2. A volume of 200 ml of KCl-saturated solution was poured into the vacuum chamber. The concentration signal was detected using an electric conductivity meter. Air was employed as lift gas. The average of five measurements was taken as the mixing time.

The velocity fields were measured using a particle image velocimetry (PIV) equipment. The equipment was manufactured by TSI with a laser voltage of 770 V. A 2-D image signal acquisition model is used to analyze and display the data. The experimental set-up includes a high-resolution CCD camera with a frame rate of 2.07 fps, PowerView™ Plus 11MP, 4 K × 2.7 K pixels resolution. The added tracer for PIV measurement consisted of hollow glass spheres with a density of 0.99 g/cm³ and a particle size of 10 μm in diameter. The number of particles was 4 to 6 per grid in the view field.

Figure 3 indicates the model results on the tracer concentration signal as a function of time and the measured value, corresponding to conditions employing four nozzles and a gas flow rate of 20 L/min. The

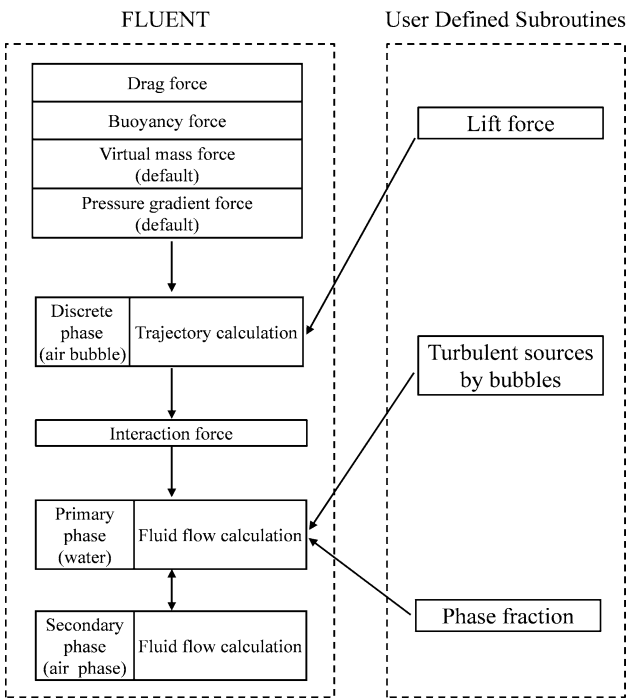


Fig. 1—Flow chart of mathematical models.

Table II. Property Parameters of Water and Air

Phase	Parameter	Value
Water	density (kg/m ³)	998.2
	viscosity (Pa s)	0.001003
Air	density (kg/m ³)	1.225
	viscosity (Pa s)	1.7894 × 10 ⁻⁵
Surface tension (N/m)		0.07197

Table III. Dimensions (Diameter and Height) of Prototype and Water Model

	Ladle			Vacuum Chamber		Snorkel	
	D_{top} (mm)	D_{bottom} (mm)	H (mm)	D (mm)	H (mm)	D (mm)	H (mm)
Prototype	3959	3324	4060	2144	8225	650	
Water model	792	665	812	481	822	130	345

Table IV. Dimensions (Diameter and Height) of Prototype and Water Model

	Prototype	Water Model
Number of nozzles	12	4, 6, 8
Gas flow rate (L/min)	1600 to 4800	12, 16, 20, 24, 28, 32, 36
Nozzle diameter (mm)	6	4

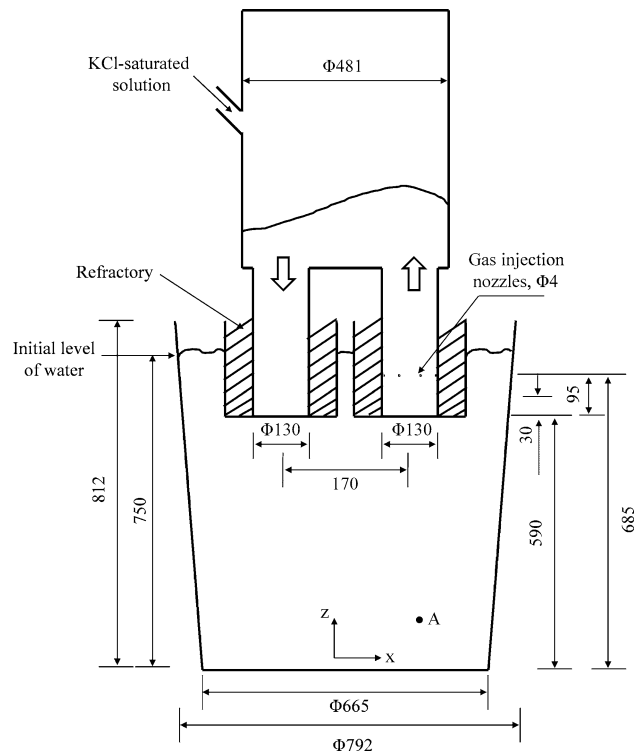


Fig. 2—Schematic of experimental RH water model.

predicted mixing time was 41.87 seconds and the measured value was 40.33 seconds. The agreement is quite satisfactory and within the margins of the standard deviation of the experimental measurements.

The velocity fields predicted by the model in two directions as shown in Figure 4 with those measured by PIV are compared in Figures 5 and 6. The liquid coming out from the down-leg snorkel firstly impinges on the bottom of the ladle, flows along the bottom, and then flows upwards along the right wall. Besides, the main flow of the liquid directly flows into the up-leg snorkel and part of the liquid turns left so that a recirculation eddy exists below the up-leg. The calculated flow pattern is consistent with the measured results. Figure 4(a) indicates velocity fields in the range from 0.01 to 0.23 m/s in the entire computational domain. Figure 5 corresponds to the velocity fields in the direction of the flow leaving the down-leg snorkel and Figure 6 corresponds to the velocity fields in a radial direction, at a height of 500 mm. These results also correspond to conditions with four nozzles and a gas flow rate of 20 L/min. It can be observed that the liquid from the down-leg snorkel is discharged at a velocity of 0.23 m/s and there is good agreement between model and measured values. As the liquid moves to the ladle's bottom, the model predicts a uniform descent in velocity. In the final section, 100 mm from the bottom, the model and measured values give a

good agreement. In this region, the velocity drops rapidly from 0.15 to 0.01 m/s. The main discrepancies between the model and the measured results are in the middle section, where the measured values drop at a faster rate, however, taking into account the overall behavior, it can be observed that the model and the measured values offer a satisfactory agreement. The comparison in velocities in the radial direction shown in Figure 6 indicates two peaks in velocities. The largest peak corresponds to the velocity of the liquid from the down-leg snorkel and the second peak to the liquid ascending to the up-leg snorkel. The velocity on the up-leg snorkel represents about 25 pct of the maximum velocity in the down-leg snorkel. The comparison between predicted and measured values in the radial direction agrees quite well, therefore, based on the previous results it is concluded that the current mathematical model provides accurate predictions of the velocity fields and mixing time.

Figure 7 shows the iso-surface when the velocity of the liquid is 0.1 m/s and the motion of the gas bubbles. The formation of liquid droplets at the free surface is observed. If the upper phase would be the slag phase, the droplet formation mechanism could be associated with slag entrainment. This result shows an improvement

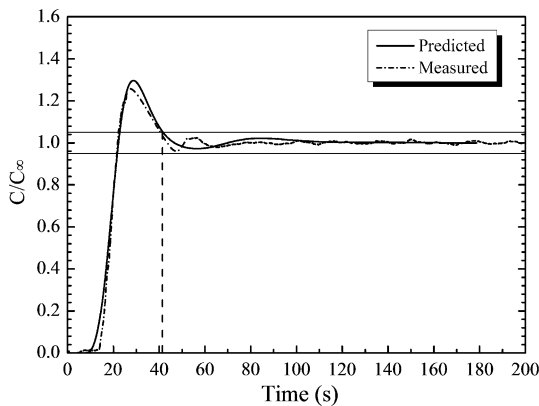


Fig. 3—Mixing time based on dimensionless concentration versus time response.

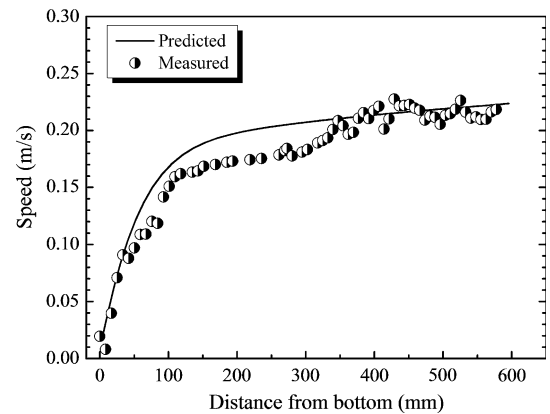


Fig. 5—Comparison in velocity distribution along the down-leg between model predictions and measured values, using four nozzles and a gas flow rate of 20 L/min.

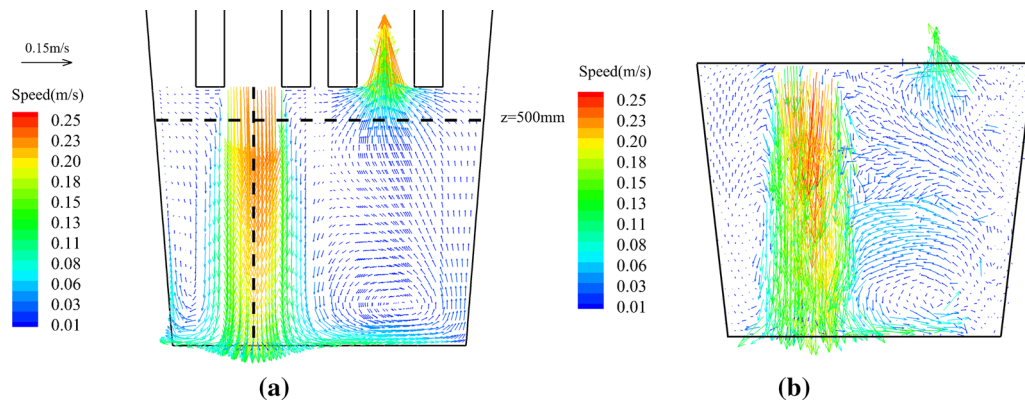


Fig. 4—Velocity fields in the ladle using four nozzles and a gas flow rate of 20 L/min (a) predicted; (b) measured.

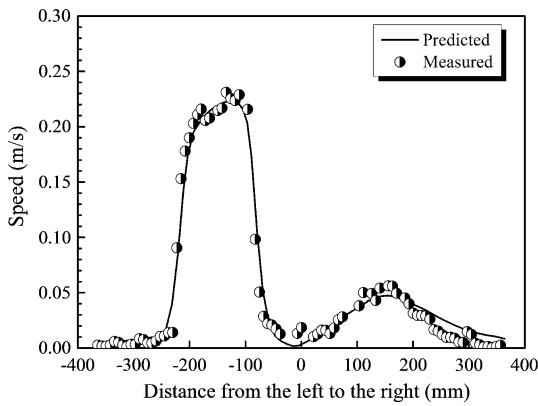


Fig. 6—Comparison in the velocity distribution along radial direction at a height of 500 mm, between model predictions and measured values, using four nozzles and a gas flow rate of 20 L/min.

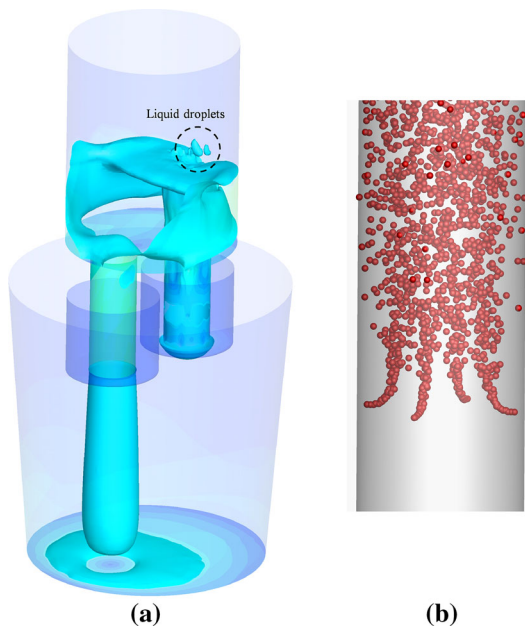


Fig. 7—Three-dimensional isometric contour of 0.1 m/s of the velocity magnitude and motion of gas bubbles, for the case of four nozzles and a gas flow rate of 20 L/min.

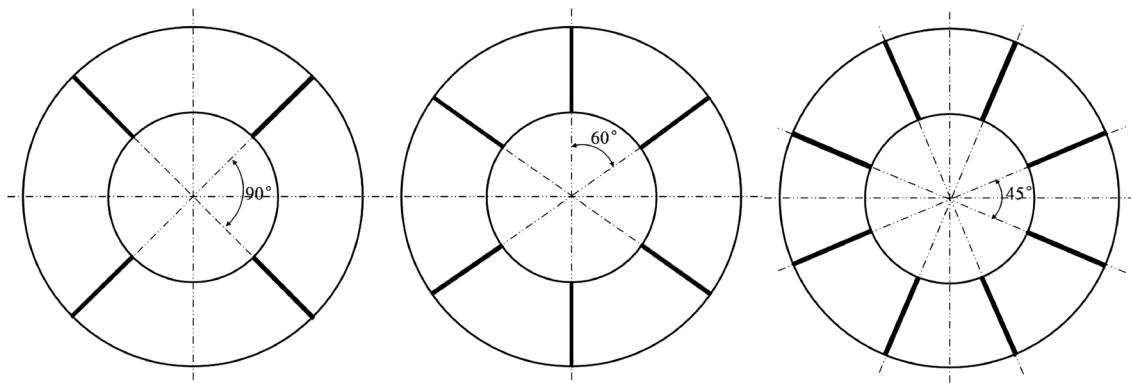


Fig. 8—Details of three different nozzle arrangements with four, six, and eight nozzles.

over previous models. A numerical model to reproduce multiphase flow and fluctuations on the free surface was recently published by Liu *et al.*^[25] in 2011. This model however shows some inconsistencies in the velocity fields because even if the gas flow rate increases, the velocity fields in the recirculation zone changes too little. This is probably due to having ignored the lift force in their modeling work.

IV. EFFECT OF THE NUMBER OF NOZZLES INJECTING GAS

A. Gas Volume Fraction

The gas volume fraction of the injected gas in the snorkel is an important parameter to understand fluid flow in the RH process, in particular to clarify the effect of the number of nozzles on recirculation rate. The nozzle configurations employed in this work are illustrated in Figure 8. In the case of four nozzles their separation angle is 90 deg, for six nozzles is 60 deg, and for eight nozzles is 45 deg. In order to describe the evolution of the gas volume fraction as a function of its traveling distance along the snorkel, cross-sectional planes over a distance of 150 mm are employed, as shown in Figure 9. Figure 10 shows the results in those planes, for the case of four nozzles and a gas flow rate of 20 L/min. This case represents in this work low mixing conditions and explains why the gas columns never mix as the gas bubbles ascend from the nozzle up to a distance of 150 mm. In this distance the gas columns expand but remain as individual gas plumes.

Figure 11 describes the gas volume and velocity fields in the up-leg snorkel for the case of four nozzles and two gas flow rates. It can be observed that at low gas flow rates (12 L/min) the plumes remain individual up to the free surface in the vacuum chamber, on the contrary, when the gas flow rate is high (36 L/min) the plumes expand and collide forming a single gas column. Geng *et al.*^[8] reported similar results for an industrial RH system when the lifting gas flow rate was low. When the number of nozzles increases from 4 to 6 and from 6 to 8, as shown in Figure 12, for a height of 775 mm, the general response is similar. Figure 13 summarizes the gas volume fraction as a function of the number of

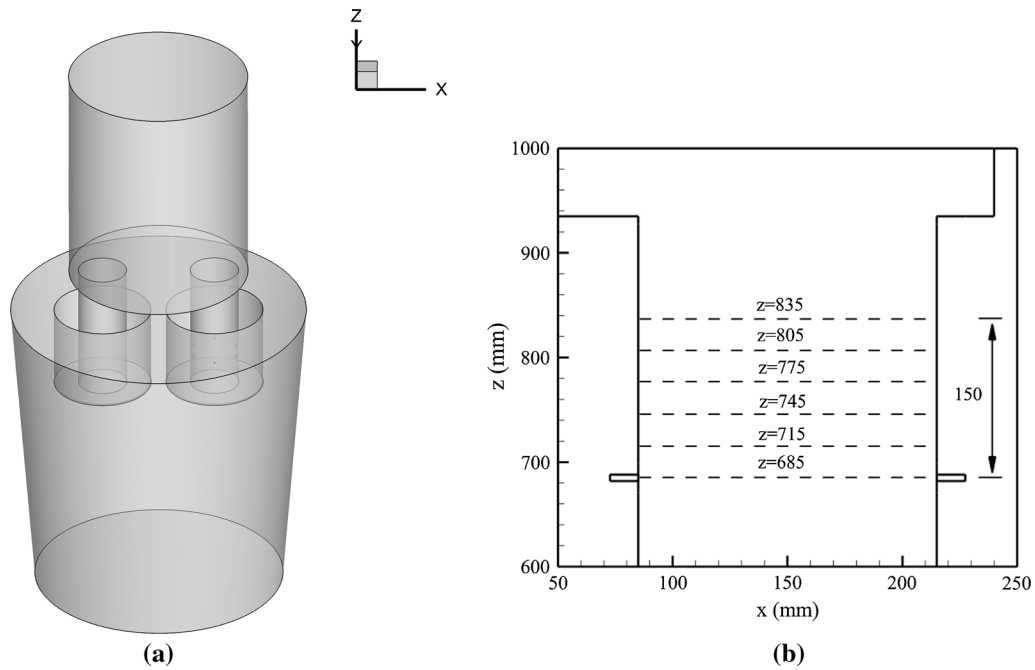


Fig. 9—(a) Snorkel geometry, (b) position of reference planes employed to analyze the gas volume fraction.

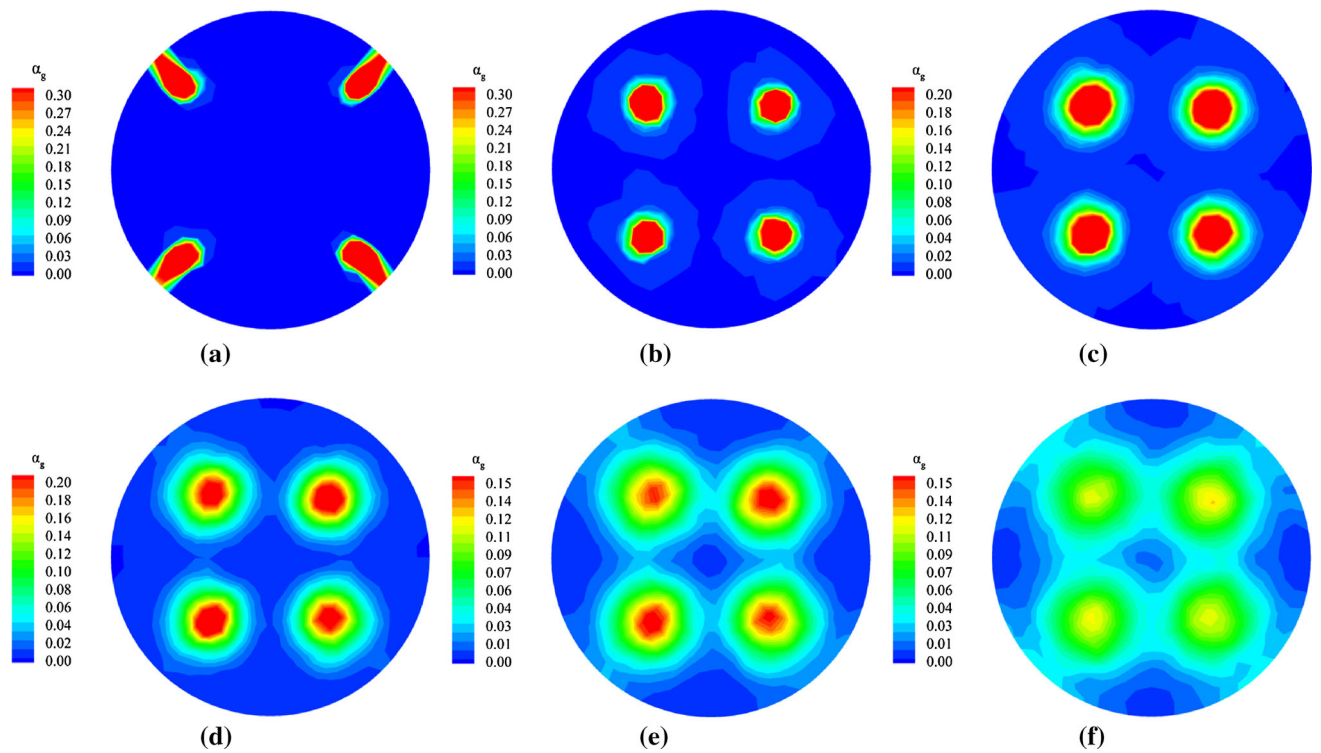


Fig. 10—Comparison of the gas volume fraction as a function of snorkel height, for the case of four nozzles and a gas flow rate of 20 L/min. (a) 685, (b) 715, (c) 745, (d) 775, (e) 805, (f) 835 mm.

nozzles. The main difference when the number of nozzles increases from 4 to 6 and 6 to 8 is in the gas penetration depth. There is a smaller gas penetration depth as the number of nozzles increases. At this height the maximum gas volume fraction is reported at a depth

of approximately 30 mm for the case of four nozzles but this value decreases to 17 mm when the number of nozzles is increased to 8. At higher gas flow rates the gas penetration depth increases and more bubbles reach the center of the snorkel.

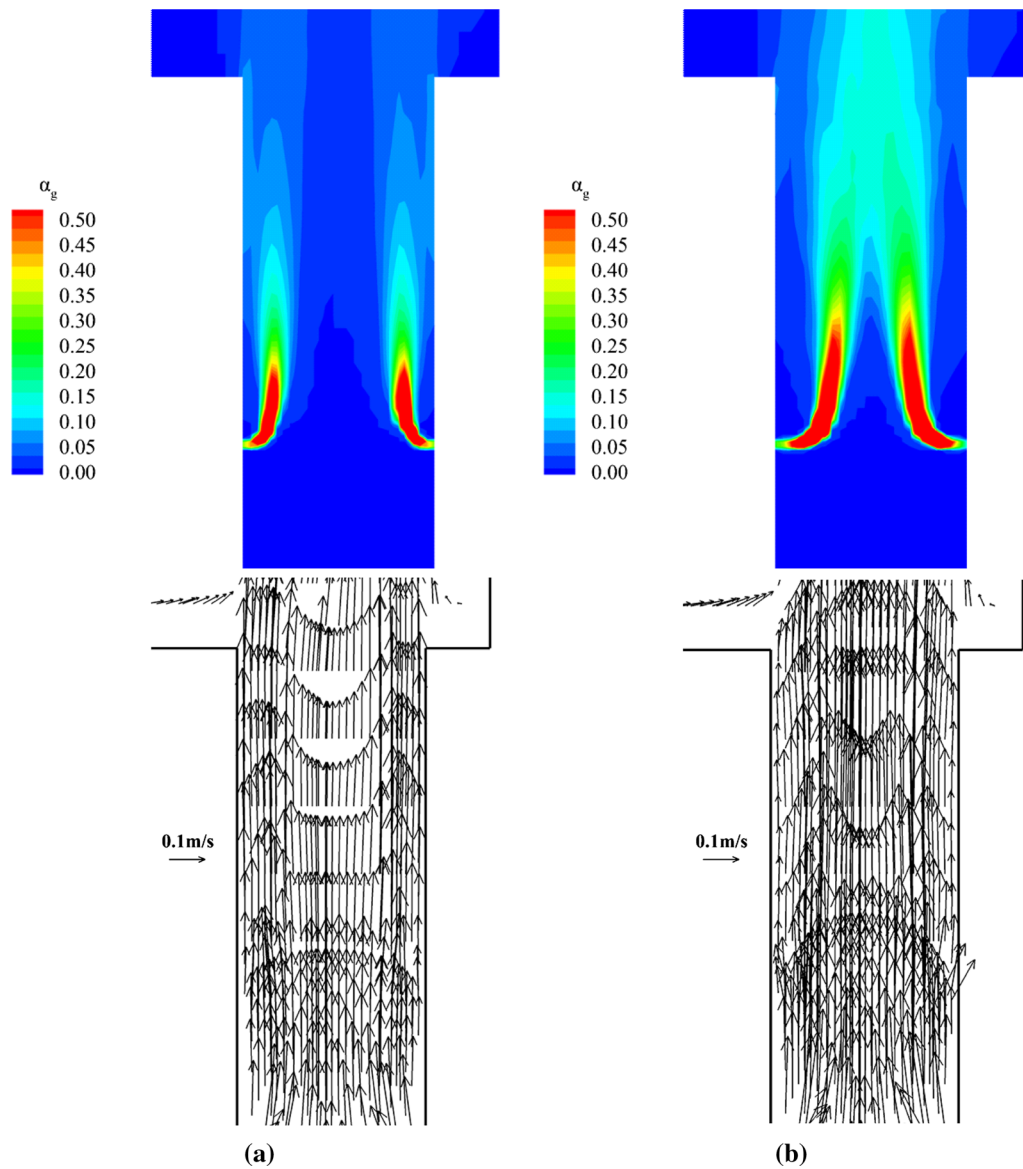


Fig. 11—Gas volume distribution and velocity fields in the up-leg snorkel for the case of four nozzles and two gas flow rates. (a) 12 L/min, (b) 36 L/min.

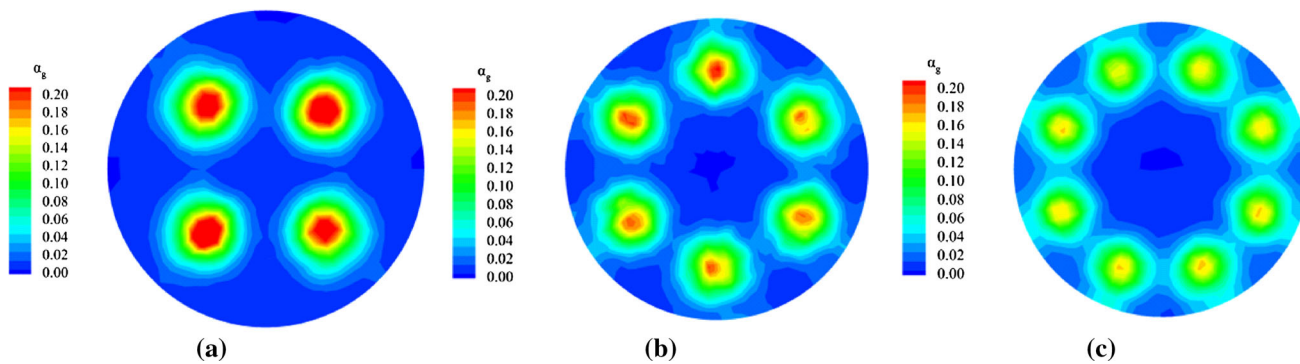


Fig. 12—Comparison of the gas volume fraction as a function of nozzle number for a gas flow rate of 20 L/min, at a height of 775 mm. (a) Four, (b) six, (c) eight nozzles.

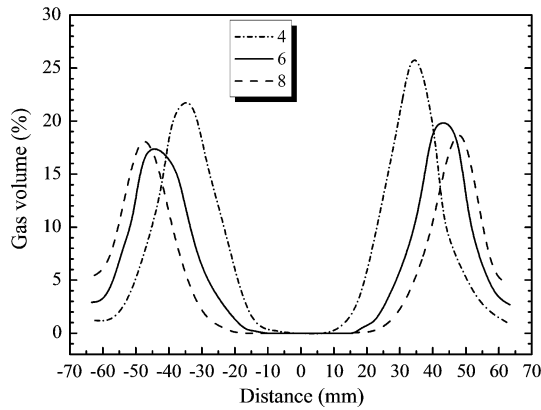


Fig. 13—Comparison of gas volume in the radial direction as a function of the number of nozzles, for a gas flow rate of 20 L/min, at a height of 775 mm.

It is clear from the previous results that the lifting gas volume in the up-leg snorkel is directly related with the velocity fields. The velocity increases as the gas volume also increases and then the recirculation rate increases.

B. Recirculation Rate and Mixing Time

The recirculation rate (in kg/s) was computed using the following equation:

$$R = \bar{u} \cdot A_o \cdot \rho_w, \quad [24]$$

where \bar{u} is the average velocity in the snorkel $\left(\frac{\sum_{i=1}^n A_i u_i}{A_o} \right)$ in m/s, u_i is the velocity in each cell and A_i is its corresponding area, A_o is the cross-sectional area in m^2 of the snorkel and ρ_w is the density of water in kg/m^3 . The velocities correspond to a height of 600 mm, close to the exit of the down-leg snorkel. The velocities are similar in both heights.

Figure 14 shows the recirculation rate as a function of gas flow rate for three nozzle configurations. It can be observed that an increase in the lifting gas flow rate increases the recirculation rate, however it tends to achieve a maximum recirculation rate at about 36 L/min. This result is in line with previous investigations.^[1,7-10] In regard with the effect of the number of nozzles, the current work has found an optimum value of six nozzles. If the number of nozzles increases to 8, the recirculation rate no longer increases but decreases. The fact that a different optimum number of nozzles has been reported in the past is an indication that the main reason is not the number itself but the combination of different variables that together produce the maximum velocity of the liquid in the up-leg snorkel. In order to provide additional elements to describe the observed behavior, the mixing time and the area of the plume in the up-leg snorkel were calculated with the model. Figure 15 shows that in general the area of the plume increases in proportion to the recirculation rate. These results are in agreement with the experimental data reported by Nascimento *et al.*^[14] With the area of the

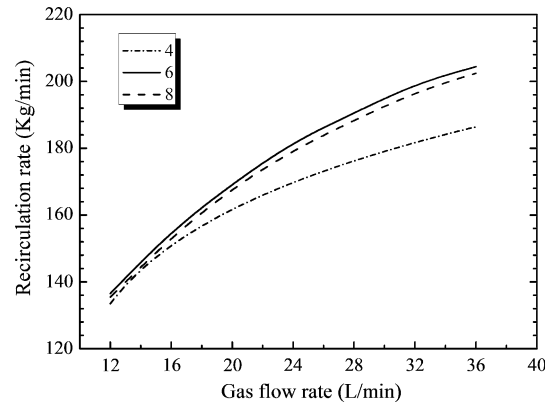


Fig. 14—Effect of gas flow rate and number of nozzles on the recirculation rate.

plume increasing, the interaction between the gas bubble and the liquid is enhanced. Thus the velocity of the liquid and the recirculation rate increase, as suggested by the study of Park *et al.*^[1] In the case of four nozzles it is also observed a decrease in the area as gas flow rate increases. This phenomena occurs when the plumes coalesce into a single one. The total area of the individual plumes is higher in comparison with only one plume.

The plume area in the up-leg snorkel calculated in this work involves regions with a volume fraction of gas larger than 2 pct. Figure 16 shows a direct relationship between the plume area (A , in pct) and recirculation rate (R in L/min), as follows:

$$R = 1.26A + 66 \quad [25]$$

Figure 17 reports the effect of gas flow rate and number of nozzles on mixing time. In line with the previous results on recirculation rate, an increase in gas flow rate decreases mixing time. The results are consistent by showing that the optimum number of nozzles in this work is 6. To improve the refining efficiency of the RH degasser, six nozzles should be adopted in the actual RH degasser. Meanwhile, the appropriate gas flow rate was in the range from 1600 to 4800 L/min in the actual RH degasser according to the modified Froude number, corresponding to the gas flow rate of 12 to 36 L/min in water modeling.

In summary, based on the results above, it is possible to provide an explanation on the mechanism that defines an optimum gas flow rate and number of nozzles to reach a large value in recirculation energy. As the gas flow rate increases or the number of nozzles increases, the gas volume fraction in the up-leg snorkel also increases. Figure 18 indicates an increase in gas volume fraction from 3 to 7 pct when the lift gas flow rate increases from 12 to 36 L/min. With a higher gas volume fraction there are more bubbles and the velocity of the liquid increases. However, as the gas flow rate or the number of nozzles increases there is critical value at which individual plumes coalesce into one large

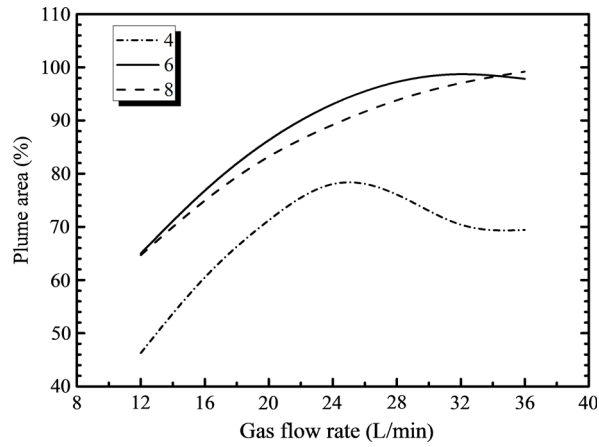
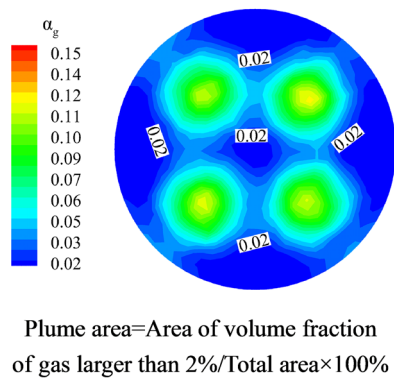


Fig. 15—Effect of gas flow rate on the plume area.

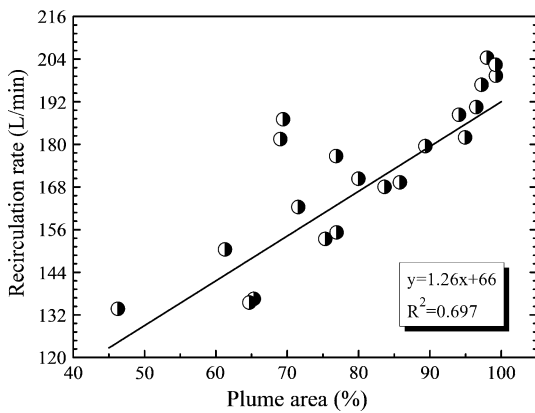


Fig. 16—Relationship between the recirculation rate and the plume area.

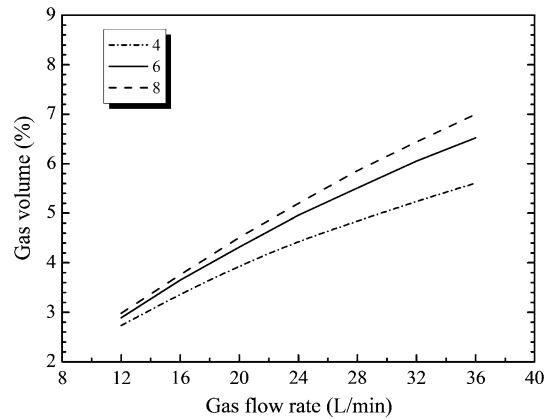


Fig. 18—Effect of gas flow rate and number of nozzles on gas volume (gas volume: the average gas volume fraction at a height of 835 mm).

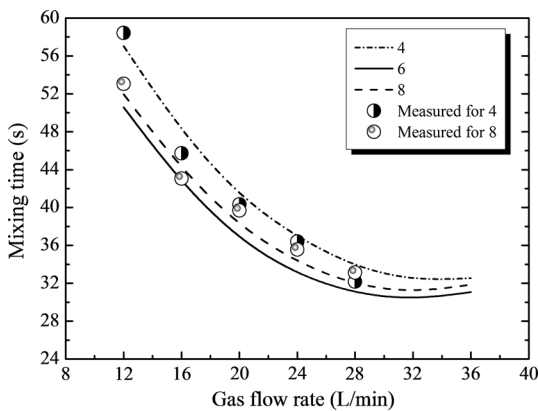


Fig. 17—Effect of gas flow rate and number of nozzles on mixing time.

plume. This is observed when the area of the plume abruptly decreases. At this point the rate of increase in velocities is less than 5 pct, as shown by the values reported in Table V. It means that the recirculation rate could still be increased but the rate of change becomes negligible.

Table V. Average Velocity in the Down-leg Snorkel as a Function of Q and N (Units: m/s)

N/Q	12 L/min	16 L/min	20 L/min	24 L/min	28 L/min	32 L/min	36 L/min
4	0.168	0.189	0.204	0.214	0.222	0.228	0.235
6	0.172	0.195	0.213	0.229	0.239	0.250	0.257
8	0.170	0.193	0.211	0.226	0.237	0.247	0.254

V. CONCLUSIONS

Mathematical models of VOF + DPM were developed to investigate the effect of the number of nozzles on the recirculation rate and mixing time in the RH process. Based on the results and discussion, the following conclusions have been reached:

1. The current mathematical model has been validated with experimental data from a water model. It is an improved model because it also includes multiphase flow accounting for the fluctuation in the free surface in the vacuum chamber.

2. As the number of nozzles increases a value is reached to achieve an optimum maximum recirculation flow rate and minimum mixing time. In the current work the optimum number of nozzles was six.
3. The mechanism that controls the optimum maximum recirculation rate by the lift gas flow rate and the number of nozzles is the formation of one single plume. In practice, this point can be defined by measuring the plume area. The critical gas flow rate or the maximum number of nozzles will give the maximum area of the plume. This point also corresponds with a deceleration in the rate of increase in recirculation rate, equivalent to less than 5 pct increment in the velocity fields.

ACKNOWLEDGMENTS

The authors are grateful for support from the National Science Foundation China (Grant Nos. 51274034 and 51404019), State Key Laboratory of Advanced Metallurgy, Beijing Key Laboratory of Green Recycling and Extraction of Metals (GREM), the Laboratory of Green Process Metallurgy and Modeling (GPM²), and the High Quality Steel Consortium (HQSC) at the School of Metallurgical and Ecological Engineering at University of Science and Technology Beijing (USTB), China.

REFERENCES

1. Y.G. Park, K.W. Yi, and S.B. Ahn: *ISIJ Int.*, 2001, vol. 41, pp. 403–09.
2. B. Li and F. Tsukihashi: *ISIJ Int.*, 2000, vol. 40, pp. 1203–09.
3. Y.G. Park, W.C. Doo, K.W. Yi, and S.B. An: *ISIJ Int.*, 2000, vol. 40, pp. 749–55.
4. L. Zhang and F. Li: *JOM*, 2014, vol. 66, pp. 1227–40.
5. K. Chattopadhyay, M. Isac, and R.I.L. Guthrie: *ISIJ Int.*, 2010, vol. 50, pp. 331–48.
6. A.N. Conejo, S. Kitamura, N. Maruoka, and S.-J. Kim: *Metall. Mater. Trans. B*, 2013, vol. 44B, pp. 914–23.
7. P.A. Kishan and S.K. Dash: *ISIJ Int.*, 2009, vol. 49, pp. 495–504.
8. D. Geng, H. Lei, and J. He: *Metall. Mater. Trans. B*, 2010, vol. 41B, pp. 234–47.
9. C. Kamata, S. Hayashi, and K. Ito: *Tetsu-to-Hagané*, 1998, vol. 84, pp. 484–89.
10. L. Neves, H.O. de Oliveira, and R.P. Tavares: *ISIJ Int.*, 2009, vol. 49, pp. 1141–49.
11. S.K. Ajmani, S.K. Dash, S. Chandra, and C. Bhanu: *ISIJ Int.*, 2004, vol. 44, pp. 82–90.
12. R. Tsujino, J. Nakashima, M. Hirai, and I. Sawada: *ISIJ Int.*, 1989, vol. 29, pp. 589–95.
13. J. Han, X. Wang, and D. Ba: *Vacuum*, 2014, vol. 109, pp. 68–73.
14. A.A. Nascimento, H.L.V. Pujatti, L. Neves, T.R.C. de Almeida, and R.P. Tavares: AISTech Proceedings, Indianapolis IN, 2007.
15. S. Li, X. Ai, N. Wang, and N. Lv: *Adv. Mater. Res.*, 2011, vols. 287–290, pp. 840–43.
16. L. Lin, Y. Bao, F. Yue, L. Zhang, and H. Ou: *Int. J. Miner. Metall. Mater.*, 2012, vol. 19, pp. 483–89.
17. S. Inoue, Y. Furuno, T. Usui, and S. Miyahara: *ISIJ Int.*, 1992, vol. 32, pp. 120–25.
18. R.K. Hanna, T. Jones, R.I. Blake, and M.S. Millman: *Ironmak. Steelmak.*, 1994, vol. 21, pp. 37–43.
19. F. Jiang and G.G. Cheng: *Ironmak. Steelmak.*, 2012, vol. 39, pp. 386–90.
20. B. Zhu, Q. Liu, D. Zhao, S. Ren, M. Xu, B. Yang, and B. Hu: *Steel Res. Int.*, 2016, vol. 87, pp. 136–45.
21. O. Davila, L. Garcia-Demedices, and R.D. Morales: *Metall. Mater. Trans. B*, 2006, vol. 37B, pp. 71–87.
22. J.W. Han, S.H. Heo, D.H. Kam, B.D. You, J.J. Pak, and H.S. Song: *ISIJ Int.*, 2001, vol. 41, pp. 1165–73.
23. B. Li, H. Yin, C.Q. Zhou, and F. Tsukihashi: *ISIJ Int.*, 2008, vol. 48, pp. 1704–11.
24. L. Zhang: *Model. Simul. Mater. Sci. Eng.*, 2000, vol. 8, p. 463.
25. H. Liu, Z. Qi, and M. Xu: *Steel Res. Int.*, 2011, vol. 82, pp. 440–58.
26. C.W. Hirt and B.D. Nichols: *J. Comput. Phys.*, 1981, vol. 39, pp. 201–25.
27. J.T. Kuo and G.B. Wallis: *Int. J. Multiph. Flow*, 1988, vol. 14, pp. 547–64.
28. S.T. Johansen and F. Boysan: *Metall. Trans. B*, 1988, vol. 19B, pp. 755–64.
29. Y.Y. Sheng and G.A. Irons: *Metall. Mater. Trans. B*, 1995, vol. 26B, pp. 625–35.
30. D. Guo and G.A. Irons: *Metall. Mater. Trans. B*, 2000, vol. 31B, pp. 1457–64.
31. K. Beskow, L. Jonsson, D. Sichen, and N.N. Viswanathan: *Metall. Mater. Trans. B*, 2001, vol. 32B, pp. 319–28.
32. J. Aoki, L. Zhang, and B. G. Thomas: ICS 2005-The 3rd International Congress on the Science & Technology of Steelmaking (Charlotte, NC, May 9–12), AIST, Warrendale. 2005.
33. M. Madan, D. Satish, and D. Mazumdar: *ISIJ Int.*, 2005, vol. 45, pp. 677–85.
34. V.D. Felice, I.L.A. Daoud, B. Dussoubs, A. Jardy, and J.P. Bellot: *ISIJ Int.*, 2012, vol. 52, pp. 1273–80.
35. J.P. Bellot, V.D. Felice, B. Dussoubs, A. Jardy, and S. Hans: *Metall. Mater. Trans. B*, 2013, vol. 45B, pp. 13–21.
36. ANSYS FLUENT 14.0. Canonsburg, PA: ANSYS, Inc. 2011.
37. B.E. Launder and D.B. Spalding: *Lectures in mathematical models of turbulence*, Academic Press, England, 1972.
38. S.A. Morsi and A.J. Alexander: *J. Fluid Mech.*, 1972, vol. 55, pp. 193–208.
39. J.F. Davidson and BOG Schüler: *Trans. Inst. Chem. Eng.*, 1960, vol. 38, pp. 335–42.
40. L. Zhang and S. Taniguchi: *Int. Mater. Rev.*, 2000, vol. 45, pp. 59–82.
41. C.G. Méndez, N. Nigro, and A. Cardona: *J. Mater. Process. Tech.*, 2005, vol. 160, pp. 296–305.
42. D.A. Drew, D.D. Joseph, and S.L. Passman: *Particulate Flows: Processing and Rheology*, Springer, 1998.
43. M. Pourtousi, J.N. Sahu, and P. Ganesan: *Chem. Eng. Process.*, 2014, vol. 75, pp. 38–47.
44. Y. Xie and F. Oeters: *Steel Res. Int.*, 1992, vol. 63, pp. 93–104.